Available online at www.sciencedirect.com
SCIENCE DIRECT®
ELSEVIER Computers and Mathematics with Applications 51 (2006) 643–660
An International Journal
computers & mathematics
with applications
www.elsevier.com/locate/camwa

Numerical Simulations of the Flow and Sound Fields of a Heated Axisymmetric Pulsating Jet

X. JIANG*, H. ZHAO AND L. CAO
Mechanical Engineering
School of Engineering and Design, Brunel University
Uxbridge UB8 3PH, U.K.
Xi.Jiang@brunel.ac.uk

(Received and accepted March 2005)

Abstract—The flow and sound fields of a heated axisymmetric pulsating jet have been investigated by direct numerical solution of the compressible Navier-Stokes equations in cylindrical coordinates using highly accurate numerical methods. Effects of pulsating frequency and amplitude on the flow structure and sound generation have been examined. The results show that the organized unsteadiness associated with the periodic pulsation leads to a variety of vortical structures in the pulsating flow field. The pulsating frequency and amplitude strongly affect the vortical flow structures and the radiated sound fields. At the higher pulsating frequency, the vortices in the pulsating jet become smaller and the radiated sound field has smaller wavelength. The pressure fluctuation amplitude of the sound field is inversely proportional to the distance from the sound source. Both the larger pulsating frequency and larger pulsating amplitude lead to stronger sound emissions from the pulsating jet. It has been found that the pressure fluctuation amplitude of the sound field is approximately proportional to the pulsating amplitude and frequency.

Keywords—Flow pulsation, Jet noise, Direct numerical simulations.

1. INTRODUCTION

Pulsating jets are encountered in a broad range of engineering and environmental applications [1–8]. One example of pulsating jets in application is the flow originated from reciprocating engines, which are used in many industrial applications such as vehicles, airplanes, vessels, and so on. For pulsating flows, one prominent feature is the strong noise generation associated with the flow pulsation. Flow pulsation occurs either due to the operating conditions of the system such as those in reciprocating engines, or due to the imposed oscillations in the system. Pulsation can considerably affect the jet expansion, mixing, and noise generation. For reciprocating engines. the tailpipe noise radiated from the pulsating flow near the open terminations of the intake and exhaust systems is a significant source of noise. For example, it accounts for more than 20% of the overall machine noise of vehicles [1].

*Author to whom all correspondence should be addressed.

0898-1221/06/$ - see front matter Typeset by AMS-TEX
doi:10.1016/j.camwa.2005.03.022

The current noise reduction measures for pulsating flows are mainly empirical. To reduce tailpipe noise, silencing systems coupled to the intake and exhaust manifolds have been used (see [1–3]). The development of acoustic silencers is generally based on extensive "build and test" experimental work to achieve an engine "breathing" at acceptable noise levels. This traditional procedure is time-consuming and expensive. The development of numerical simulation models, however, provides predictive analysis of noise generation, which can play a very effective role in developing noise reduction measures to achieve the required noise characteristics.

The noise generation from pulsating flows represents a challenging problem because the flow is highly unsteady, vortical with intermittency and compressible in many applications. The discharged pulsating flow is also of a multidimensional nature. Due to the complexities involved, the noise generation from the discharged pulsating flows has not been fully understood. A better understanding on the sound generation from pulsating jets can help to achieve effective noise control of pulsating flows via active and passive measures. In general, the predictive software available for engine noise does not provide quantitative estimates of the contributions by flow noise to the orifice sound emissions [9]. The traditional computational fluid dynamics (CFD) based on Reynolds-averaged Navier-Stokes turbulence modelling is not suitable for predicting the highly unsteady and vortical pulsating flows due to the inherent time-averaging involved. The numerical accuracy of traditional CFD is also too low to predict noise generation.

As a new computational aeroacoustics (CAA) approach, direct numerical simulations (DNS) provide detailed information on sound generation by resolving all the relevant time and length scales. To date, a systematic study of noise generation from the discharged pulsating flows using advanced CAA approaches such as DNS has not been performed. The pulsating flows involve the coupling between velocity and pressure fluctuations. The highly accurate methods in DNS can predict the flow field and sound field simultaneously to yield in-depth knowledge about the noise generation from pulsating flows that consists of transient compression and expansion waves, which is not achievable using the traditional CFD approach.

For pulsating jets, the pulsating frequency and amplitude are important flow control parameters. In practical applications, effective control of these two parameters can play a significant role in achieving the desired heat and mass transfer properties and noise emission characteristics of the jet. Due to the complexity of the problem and the lack of powerful tools to investigate the flow unsteadiness and the coupling involved, there is currently a lack of fundamental knowledge on the sound generation from pulsating jets particularly the effects of pulsating frequency and amplitude. Direct computation provides a possibility to investigate these effects thoroughly by fully resolving the unsteadiness and vortical structures in pulsating jets.

In literature, no previous work had been conducted for the detailed effects of pulsating frequency and amplitude on noise emission characteristics of pulsating jets. This study was motivated to understand the noise generation mechanisms of pulsating jets and the effects of pulsating amplitude and frequency on the flow structures and noise generation from pulsating flows. Numerical simulations have been performed based on a recently developed CAA code for noise generation from axisymmetric jets [10–12]. The code used is highly accurate with sixth-order numerical accuracy for spatial differentiation and third-order accuracy for time advancement. An acoustic analogy analysis of the sound source structure in the pulsating jet has also been performed. A comparative numerical study has been performed for a heated axisymmetric jet with nondimensional pulsating frequencies of 0.1, 0.2, and 0.5, and pulsating amplitudes of 100%, 50%, and 10%, respectively. The results obtained from the simulations performed provide detailed information on the vortical flow and sound source structures and sound fields of the pulsating jet.

2. MATHEMATICAL FORMULATION

The physical problem considered is a heated pulsating jet issuing into an open boundary domain, which has been described by the compressible Navier-Stokes equations in cylindrical

coordinates. The pulsating jet emits sound after leaving the nozzle. In this study, the non-linearized Lilley's third-order acoustic analogy equation [13] has been used to analyse the sound source structure. To ease the prohibitively high computational burden of computing the jet flow and sound fields together, only the axisymmetric case has been considered in this study. Although small-scale turbulence is prohibited in the idealized axisymmetric formulation, the simulations performed are "building blocks" for the study of fully three-dimensional turbulent jets. The mathematical formulation of the physical problem includes the governing equations for the axisymmetric jet including the flow and acoustic analogy equations, and the highly accurate numerical solution methods employed to solve the governing equations, which are described as follows.

2.1. The Flow and Acoustic Analogy Equations for the Axisymmetric Jet

For the heated axisymmetric jet, the flow field is described with the compressible time-dependent Navier-Stokes equations. The physical space is spanned by a cylindrical coordinate system (x, r, θ), where x is along the jet axis in the streamwise direction and r is the radial direction (cross-streamwise direction). In the idealized axisymmetric case considered, the jet is uniform in the azimuthal direction, that is $u_\theta = 0$. In this work, the nondimensional form of the governing equations is employed. Major reference quantities used in the normalization are the mean centerline streamwise velocity at the jet nozzle exit (domain inlet), jet radius, and the ambient temperature, density and viscosity. The nondimensional conservation laws for mass, momentum and energy can be written in the following vector form,

$$\frac{\partial \mathbf{Q}}{\partial t} = -\frac{\partial \mathbf{E}}{\partial x} - \frac{1}{r}\frac{\partial (\mathbf{F}r)}{\partial r} - \mathbf{G}, \tag{1}$$

where the vectors $\mathbf{Q}$, $\mathbf{E}$, $\mathbf{F}$, and $\mathbf{G}$ are defined as

$$\mathbf{Q} = \begin{pmatrix} \rho \\ \rho u_x \\ \rho u_r \\ E_T \end{pmatrix}, \tag{2}$$

$$\mathbf{E} = \begin{bmatrix} \rho u_x \\ \rho u_x^2 + p - \tau_{xx} \\ \rho u_x u_r - \tau_{xr} \\ (E_T + p)u_x + q_x - u_x \tau_{xx} - u_r \tau_{xr} \end{bmatrix}, \tag{3}$$

$$\mathbf{F} = \begin{bmatrix} \rho u_r \\ \rho u_x u_r - \tau_{xr} \\ \rho u_r^2 + p - \tau_{rr} \\ (E_T + p)u_r + q_r - u_r \tau_{rr} - u_x \tau_{xr} \end{bmatrix}, \tag{4}$$

and

$$\mathbf{G} = \begin{pmatrix} 0 \\ 0 \\ \dfrac{-p + \tau_{\theta\theta}}{r} \\ 0 \end{pmatrix}. \tag{5}$$

In the above equations, $E_T = \rho[e + (u_x^2 + u_r^2)/2]$ is the total energy with e standing for the internal energy per unit mass, p stands for pressure, t for time, u for velocity component, and ρ for density.

At the jet centerline, the governing equations have been put into a special form to circumvent the singularity associated with the cylindrical coordinates, which were derived from the original equations using l'Hôpital rule. The inclusion of the jet centerline into the mathematical formulation has the advantage of applying the symmetry conditions precisely. The new set of governing equations at the jet centerline can be expressed in a vector form as

$$\frac{\partial \mathbf{Q}}{\partial t} = -\frac{\partial \mathbf{E}}{\partial x} - \frac{\partial \mathbf{F}}{\partial r} - \frac{\partial \mathbf{H}}{\partial r}, \tag{6}$$

where the vector $\mathbf{H}$ is defined as

$$\mathbf{H} = \begin{bmatrix} \rho u_r \\ \rho u_x u_r - \tau_{xr} \\ \rho u_r^2 - \tau_{rr} + \tau_{\theta\theta} \\ (E_T + p)u_r + q_r - u_r\tau_{rr} - u_x\tau_{xr} \end{bmatrix}. \tag{7}$$

In equations (3)–(5) and (7), the constitutive relations for viscous stress components are $\tau_{xx} = -2/3\,\mu/\mathrm{Re}\,(-2\frac{\partial u_x}{\partial x} + \frac{\partial u_r}{\partial r} + u_r/r)$, $\tau_{rr} = -2/3\,\mu/\mathrm{Re}\,(\frac{\partial u_x}{\partial x} - 2\frac{\partial u_r}{\partial r} + u_r/r)$, $\tau_{\theta\theta} = -2/3\,\mu/\mathrm{Re}\,(\frac{\partial u_x}{\partial x} + \frac{\partial u_r}{\partial r} - 2u_r/r)$, and $\tau_{xr} = \mu/\mathrm{Re}\,(\frac{\partial u_r}{\partial x} + \frac{\partial u_x}{\partial r})$, while the heat flux components are $q_x = -\mu/[(\gamma-1)\mathrm{M}^2\,\mathrm{Pr}\,\mathrm{Re}]\frac{\partial T}{\partial x}$ and $q_r = -\mu/[(\gamma-1)M^2\,\mathrm{Pr}\,\mathrm{Re}]\frac{\partial T}{\partial r}$, respectively. Here, T stands for temperature, symbols M, Pr, and Re represent Mach number, Prandtl number, and Reynolds number respectively, μ stands for dynamic viscosity. At the jet centerline, the singularity of these constitutive relations can also be circumvented by applying l'Hôpital rule to the term u_r/r.

The governing equations also include the perfect gas law, which is given by

$$p = \frac{\rho T}{\gamma \mathrm{M}^2}. \tag{8}$$

In this study, Lilley's third-order wave equation [13] has been utilized to analyze the sound source structure. This equation can be obtained by combining the equations describing conservation of mass and momentum for compressible flow. The nonlinearized Lilley's equation has been adopted in order to avoid the ambiguity associated with the assumption of a time-independent parallel mean flow for the jet. Defining a logarithmic pressure variable $\Pi = \ln(p/p_a)$ with p_a stands for the ambient pressure, Lilley's equation in the axisymmetric cylindrical coordinates can be derived as

$$\begin{aligned} \frac{D}{Dt}\left[\frac{D^2\Pi}{Dt^2} - \frac{1}{r}\frac{\partial}{\partial x_i}\left(rc^2\frac{\partial \Pi}{\partial x_i}\right)\right] + 2\frac{\partial u_i}{\partial x_j}\frac{\partial}{\partial x_i}\left(c^2\frac{\partial \Pi}{\partial x_j}\right) + 2c^2\frac{u_r}{r^2}\frac{\partial \Pi}{\partial r} \\ = -2\gamma\frac{\partial u_i}{\partial x_j}\frac{\partial u_k}{\partial x_i}\frac{\partial u_j}{\partial x_k} - 2\gamma\frac{u_r^3}{r^3}, \end{aligned} \tag{9}$$

where $D/Dt = \frac{\partial}{\partial t} + u_i\frac{\partial}{\partial x_i}$ is the convective derivative, c is the sonic speed, γ is the ratio of specific heats. For the axisymmetric flow, the convective derivative is given by $D/Dt = \frac{\partial}{\partial t} + u_x\frac{\partial}{\partial x_x} + u_r\frac{\partial}{\partial x_r}$. The different terms in equation (9) for the axisymmetric flow can be found in a previous paper [12]. The left-hand side of the above equation is considered to be the wave operator that contains the pressure variable Π, while the right-hand side is taken as the sound source. By applying l'Hôpital's rule, the singularity of the above equation at $r = 0$ can also be circumvented [12]. In the direct simulations performed in this study, the right-hand side of equation (9) has been calculated to analyze the sound source structure of the pulsating jet.

2.2. Numerical Solution Methods

The solution methods of the governing equations include the high-order numerical schemes for time advancement and spatial discretization. The time-dependent governing equations are

integrated forward in time using a fully explicit low-storage Runge-Kutta scheme [14]. Spatial differentiation is performed by using the high-order compact (*Padé*) finite-difference scheme [15] that is of sixth order at inner points, of fourth order at the next to boundary points, and of third order at the boundary. By applying the symmetry conditions to both the primitive variables and their first and second derivatives in the radial direction, the numerical scheme has been extended to achieve the formal sixth-order accuracy at the jet centerline, which is a boundary of the computational domain.

For the computational domain, there are four boundaries that represent half of a cross-section of the axisymmetric jet, including:

(1) the symmetric boundary at the jet centerline $r = 0$;
(2) the far side boundary in the radial direction $r = L_r$;
(3) an inflow boundary at the domain inlet $x = 0$; and
(4) an outflow boundary downstream of the computational domain $x = L_x$.

At the jet centerline, symmetry conditions are applied. Nonreflecting characteristic boundary conditions [16] are used at the far side boundary in the radial direction and the outflow boundaries in the streamwise direction. For the outflow boundary, a sponge layer next to it has also been used to control the spurious wave reflections from the outside of the computational domain. The strategy of using a sponge layer at the end of the domain is similar to that of the "sponge region" or "exit zone" [17], which has been proved to be very effective to control the wave reflections through the outflow boundary. The results in the sponge layer are not truly physical and therefore are not used in the data analysis. Among the four boundaries, the inflow boundary that specifies the flow pulsation needs particular attention.

The time-dependent velocity profile of the pulsating jet at the inlet is specified based on the mean velocity and an additional sinusoidal pulsating component, given by

$$u_x = \bar{u}_x \left[1 + A \sin\left(2\pi f_0 t\right)\right], \tag{10}$$

where A stands for pulsating amplitude and f_0 stands for the nondimensional pulsating frequency applied at the inflow. A hyperbolic tangent mean velocity profile is specified at the inlet $x = 0$, which is given by

$$\bar{u}_x = \frac{1}{2}\left\{1 - \tanh\left[\frac{1}{4\delta_2}\left(r - \frac{1}{r}\right)\right]\right\}, \tag{11}$$

where $\delta_2 = 0.1$ is chosen to be the initial momentum thickness [18]. In equation (11), a tiny value 10^{-9} of r is used at the jet centerline instead of a zero value. The inlet temperature profile is specified by the Crocco-Busemann relation [19]. In the simulations performed, the flow field is initialized with the longitudinal velocity profile given in equation (11) and the inlet temperature profile, while the initial radial velocity is taken as zero. Initially, the pressure field is assumed to be uniform. For the heated pulsating jet, the temperature profile at the domain inlet has been kept unchanged during the flow pulsation. The Navier-Stokes characteristic boundary condition (NSCBC) developed by Poinsot and Lele [20] has been utilized for the specification of the inflow boundary condition. The NSCBC associated with the high-order nondissipative numerical algorithms uses the correct number of boundary conditions required for well posedness of Navier-Stokes equations that can avoid numerical instabilities and spurious wave reflections at the computational boundaries. In NSCBC, the local one-dimensional inviscid (LODI) relations [20] have been used to provide compatible relations between the physical boundary conditions and the amplitudes of characteristic waves crossing the boundary. For the pulsating inflow, the amplitudes of characteristic waves at the inflow boundary are estimated by the LODI system for the periodic pulsating streamwise velocity profile and constant temperature profile. Numerical simulations show that the NSCBC provides physical conditions for the pulsating inflow without causing numerical oscillations near the inflow boundary.

Table 1. The computational cases.

	Case A	Case B	Case C	Case D	Case E
Pulsating frequency f_0	0.1	0.2	0.2	0.2	0.5
Pulsating amplitude A	100%	100%	50%	10%	100%

3. NUMERICAL RESULTS AND DISCUSSION

Several computational cases have been performed with different pulsating frequencies and amplitudes. The code used in this study has been previously tested and validated for sound generation from subsonic axisymmetric jets [10–12]. In the following sections, results will be shown for five cases with nondimensional pulsating frequencies of 0.1, 0.2, and 0.5, and pulsating amplitude of 100%, 50%, and 10%, respectively. Table 1 summarizes these five computational cases performed. In the simulations, the considered jet Mach number is M = 0.4, which is based on the mean centerline streamwise velocity at the domain inlet (jet nozzle exit) and other reference quantities specified in the previous section. The Reynolds number based on the jet radius at the inlet is Re = 2500 and the Prandtl number used is Pr = 1. The ratio of specific heats used is $\gamma = 1.4$. For the hot jet considered, there is a temperature ratio of $T_0/T_a = 2$ at the inlet, where subscripts 0 and a represent the center of the domain inlet (jet nozzle exit) and the ambient environment, respectively. The dynamic viscosity is chosen to be temperature-dependent according to

$$\mu = \mu_a \left(\frac{T}{T_a}\right)^{0.76}$$

with the reference viscosity taken to be the ambient value.

The dimensions of the computational box used are $L_x = 80r_0$ with $L_{xs} = 70r_0$, and $L_r = 70r_0$, where $L_{xs} < x \leq L_x$ is the sponge layer. The grid system used is of 2001 × 660 nodes with a uniform distribution in the streamwise direction. In the radial direction, the grid is stretched in the hydrodynamic region to include a sufficient number of points in the jet shear layer, while it is uniformly spaced far away from the hydrodynamic region to avoid the possible distortion of the sound field by the grid stretching [12]. In this study, grid independence test has been performed and further refinement of the grid does not lead to appreciable changes in the flow or the sound field solution. The time step is limited by the Courant-Friedrichs-Lewy (CFL) condition for stability. A CFL number of 2.0 is used, which has been tested to give time-step independent results. Therefore, the results presented next are considered to be grid and time-step independent, which will be discussed in terms of the effects of pulsating frequency and amplitude on the instantaneous flow and sound field structures including time traces of the sound and the Fourier spectra, and time-averaged flow properties and sound fields including the sound source structure.

3.1. Instantaneous Flow and Sound Characteristics

The heated axisymmetric jet exhibits a periodic behaviour due to the periodic velocity pulsation applied at the inflow boundary. Figure 1 shows the instantaneous streamwise velocity profiles at $r = 1$ within the jet shear layer during one pulsating period of Case B. The periodic behaviour of the pulsating jet is obvious by comparing Figures 1a and 1d, which show an almost identical instantaneous velocity profile. In Figure 1, the velocity fluctuation of the pulsating jet is evident. The jet receives the velocity pulsation applied at the inflow boundary and the velocity variation decays significantly downstream. Although the pulsating jet has a 100% velocity pulsation at the inflow, the downstream streamwise velocity approaches a constant value due to the decay of flow pulsation in the streamwise direction for this case.

A variety of vortical structures have been observed in the pulsating flow fields from the simulations performed. In the axisymmetric flow, only the azimuthal vorticity $\omega_\theta = \frac{\partial u_r}{\partial x} - \frac{\partial u_x}{\partial r}$ is

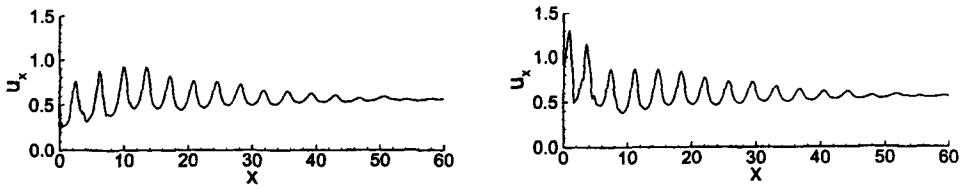

(a). $t = 200$. (b). $t = 201.67$.

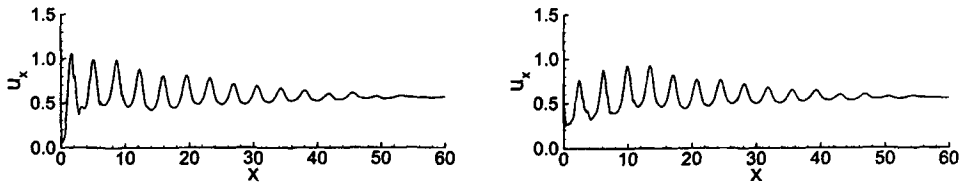

(c). $t = 203.33$. (d). $t = 205$.

Figure 1. Instantaneous streamwise velocity profiles at $r = 1$ during one pulsating period of Case B.

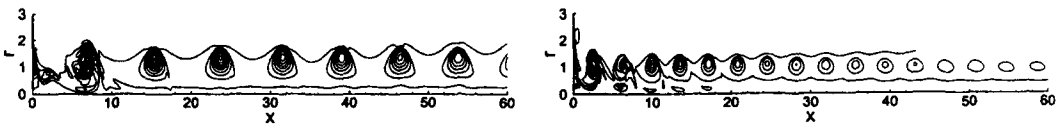

(a). Case A. (b). Case B.

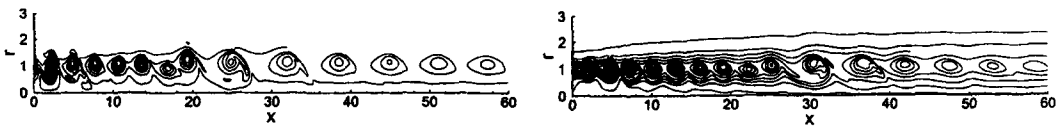

(c). Case C. (d). Case D.

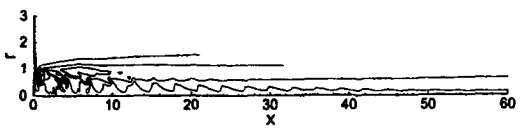

(e). Case E.

Figure 2. Instantaneous vorticity contours of Cases A–E at $t = 200$ (15 contours between the minimum and maximum values).

nonzero. In this study, the azimuthal vorticity has been calculated to examine the vortical flow field of the pulsating jet. Figure 2 shows the instantaneous vorticity contours of the five cases at $t = 200$. In order to display the vortical structures clearly, different coordinate scales have been used for the streamwise and cross-streamwise directions in the contour plots shown. From Figure 2, various "vortex puffs" associated with the formation and convection of large-scale vortical structures have been observed. The differences in the vortical flow fields among the five cases are evident in Figure 2. In this figure, the comparison between Cases A, B, and E highlights the effects of pulsating frequency on the flow structure of the heated axisymmetric jet, while the comparison among Cases B, C, and D highlights the effects of pulsating amplitude.

For jets, it is well known that there exists a preferred frequency at which an axisymmetric disturbance receives maximum amplifications in the jet column and the jet develops large-scale vortical structures [21,22]. Depending on the flow conditions, the preferred modes for unheated jets correspond to Strouhal numbers in the range of $St = 0.3 \sim 0.5$ with the most commonly

reported value at $St = 0.3$ [22], where the Strouhal number is based on the jet diameter. Since the reference length scale in this study is the jet radius, the jet preferred mode should correspond to a nondimensional frequency range of $St = 0.15 \sim 0.25$. For a heated jet, the jet preferred mode occurs at a lower frequency compared with unheated jets [23]. In this study, the pulsating frequencies applied at the inflow are close to the jet preferred mode instability. The results in Figure 2 clearly show that the pulsating jet has responded to the velocity variation at the inflow and large-scale vortical structures are developed in the flow field. For different pulsating frequencies and amplitudes applied at the inflow, the axisymmetric jet displays significantly different vortical flow structures.

For the comparison among Cases A, B, and E in Figure 2, it can be seen that the vortical structures of Case A are very large in the streamwise direction. The large "vortex puffs" observed are mainly associated with the low pulsating frequency $f_0 = 0.1$ of this case. In a periodically steady-state vortical flow, the distance between two vortex centroids can be approximated as $\lambda_1 = \bar{u}/f$, where $\bar{u}$ stands for the mean convection speed and f for the frequency of the periodic flow. Comparing Figures 2a and 2b, it can be seen that the vortex size of Case B is about a half of that of Case A in the streamwise direction. This is because the pulsating frequency of Case B is twice of that of Case A. The higher pulsating frequency leads to smaller vortex distance as shown by $\lambda_1 = \bar{u}/f$. For Case E, shown in Figure 2e with an even higher pulsating frequency, the vortex becomes much smaller that ultimately disappear downstream of the flow field. For the sake of brevity, Case E will not be discussed in detail in the following.

For the comparison among Cases B, C, and D with pulsating amplitudes of 100%, 50%, and 10% shown in Figures 2b, 2c, and 2d, respectively, an important feature is that the vortices become larger downstream for Cases C and D with smaller pulsating amplitudes compared with Case B with the larger pulsating amplitude. This is due to the vortex pairing [24,25] occurred near the end of jet potential core in Cases C and D. For a perturbed jet with the frequency of perturbation within the range of jet preferred mode instability, the shear layer can roll up and undergo successive interactions such as pairing and tearing. It has been understood that two co-rotating vortices of like-sign can merge to form a single vortex [25]. During the vortex merging, the two centroids of the co-rotating vortices are readily pushed towards each other by the local velocity field. From Figure 2, it is evident that vortex pairing/merging occurs for Cases C and D. For Case B with the strongest pulsation, the vortex pairing/merging does not occur. This is because the 100% pulsation at the inflow of this case dominates the flow field that prevents the development of vortex merging/pairing. Comparing Figures 2c and 2d, it is also observed that the vortex merging occurs further downstream with decreased pulsating amplitude.

To quantitatively compare the pulsating flow fields of different cases, Figure 3 shows the instantaneous vorticity profiles at $r = 1$ of Cases A–D at $t = 200$. It clearly shows the vortical behaviour of the pulsating flow. From Figure 3, it can be observed that the vorticity fluctuation does not change appreciably in the streamwise direction for Case A, while it decays significantly for Case B. This indicates that the heated axisymmetric pulsating jet is more susceptible to the lower frequency pulsation with $f_0 = 0.1$ than the higher frequency pulsation with $f_0 = 0.2$. The presence of vortices depends on the interaction between the flow instability and convection due to mean flow. At the higher pulsating frequency, the convection speed of the mean flow does not match the fast variation of inflow velocity pulsation; consequently, the downstream flow tends to be less susceptive to the pulsation at the higher frequency. For the comparison among Cases B, C, and D, it can be seen that decreasing the pulsating amplitude leads to smaller vorticity fluctuations. Compared with Case B, the vorticity fluctuates differently for Cases C and D downstream of the vortex pairing location due to the vortex merging occurred in these two cases.

To further examine flow characteristics of the pulsating jet, Figure 4 shows the instantaneous centerline velocity and pressure profiles of Cases A and B at $t = 200$, while Figure 5 shows the corresponding temperature and density profiles of these two cases. At the jet centerline, the streamwise velocity shown in Figure 4 clearly indicates the pulsating behaviour of the flow,

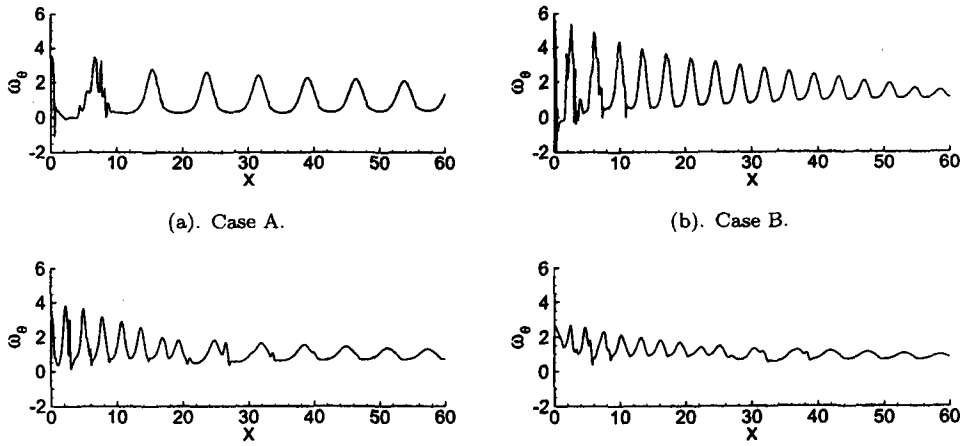

(a). Case A. (b). Case B.

(c). Case C. (d). Case D.

Figure 3. Instantaneous velocity profiles at $r = 1$ of Cases A–D at $t = 200$.

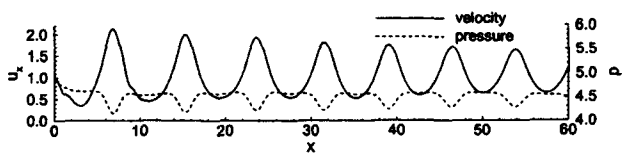

(a). Case A.

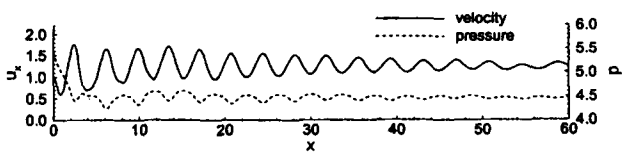

(b). Case B.

Figure 4. Instantaneous centerline streamwise vorticity and pressure profiles of Cases A and B at $t = 200$.

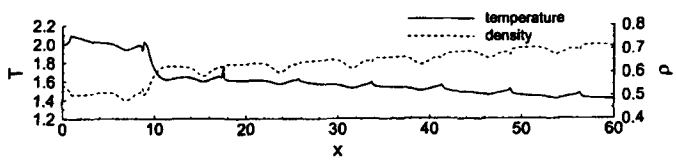

(a). Case A.

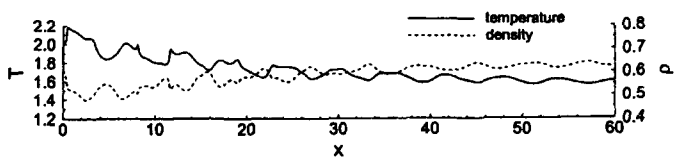

(b). Case B.

Figure 5. Instantaneous centerline temperature and density profiles of Cases A and B at $t = 200$.

where the flow radial velocity is zero due to the symmetry condition applied. The instantaneous centerline pressure distribution generally shows an opposite trend as the streamwise velocity. High velocity corresponds to low pressure due to the fact that pressure gradients drive the flow velocity.

From Figure 5, it can be observed that the temperature and density change correspondingly, but with an opposite trend. This is mainly because of the relatively low Mach number of the flow. For a Mach number M = 0.4, the flow compressibility is not significant; therefore, the pressure in the flow field does not change appreciably when the flow is fully developed. Consequently, the temperature and density change correspondingly and oppositely according to the equation of state. From Figure 5, it also can be observed that the temperature decreases in the streamwise direction due to the mixing of the hot jet with the cold ambient. The simulations show that the lower pulsating frequency leads to stronger jet mixing with the ambient and faster decay of temperature in the streamwise direction.

Sound radiation from jets is strongly associated with the large-scale vortical structures in the flow field [10–12,17,23]. Figure 6 shows the instantaneous sound fields of Cases A–D at $t = 200$, corresponding to the vorticity fields shown in Figures 2a–2d. It can be seen that the propagating acoustic fields produced by the pulsating jet are highly directive. The sound is primarily beamed with a distinctive angle relative to the jet axis. This can be attributed to the long axial length of the sound source, which leads to a highly directive or superdirective sound field [26]. From Figure 6, it is also observed that the sound wavelength of Case A with the lower pulsating frequency is longer than that of Case B with the higher pulsating frequency. For Cases B, C, and D with the same pulsating frequency, it can be seen that there is no significant difference in the sound wavelength. This is due to the fact that the sound wavelength λ_2 is mainly decided by the frequency, as indicated by $\lambda_2 = c/f$. This trend is more evident in Figure 7, which shows the instantaneous pressure fluctuation profiles at three different radial locations $r = 15$, $r = 30$, and $r = 60$ of Cases A–D at $t = 200$, corresponding to the contours of the sound fields shown in Figure 6.

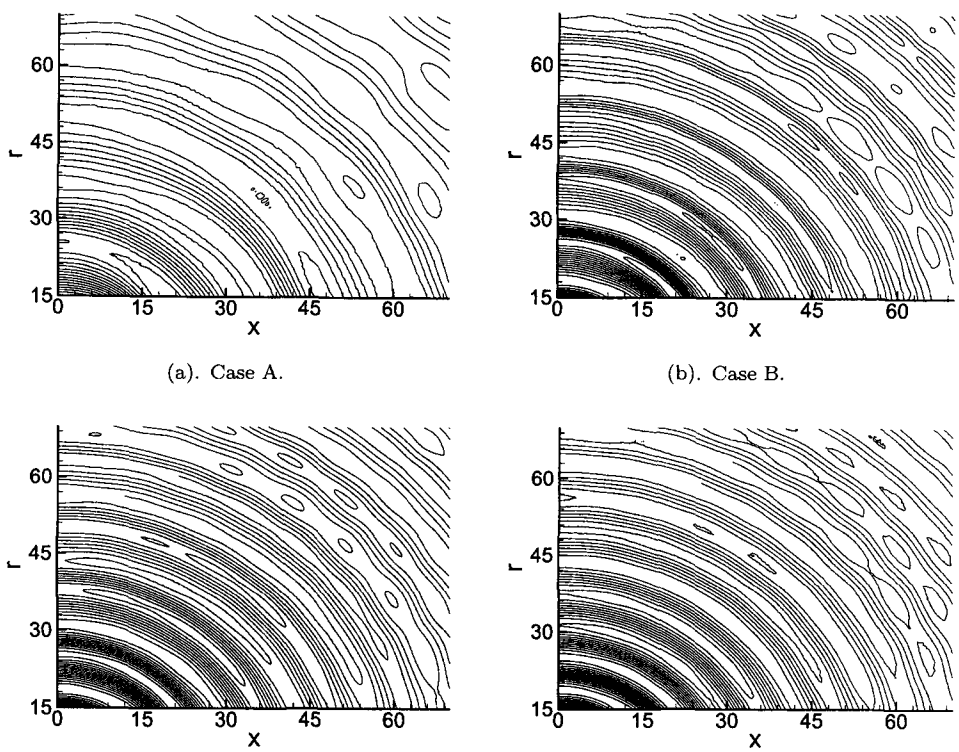

(a). Case A. (b). Case B.

(c). Case C. (d). Case D.

Figure 6. Instantaneous sound fields of Cases A–D at $t = 200$ (15 contours between the minimum and maximum values).

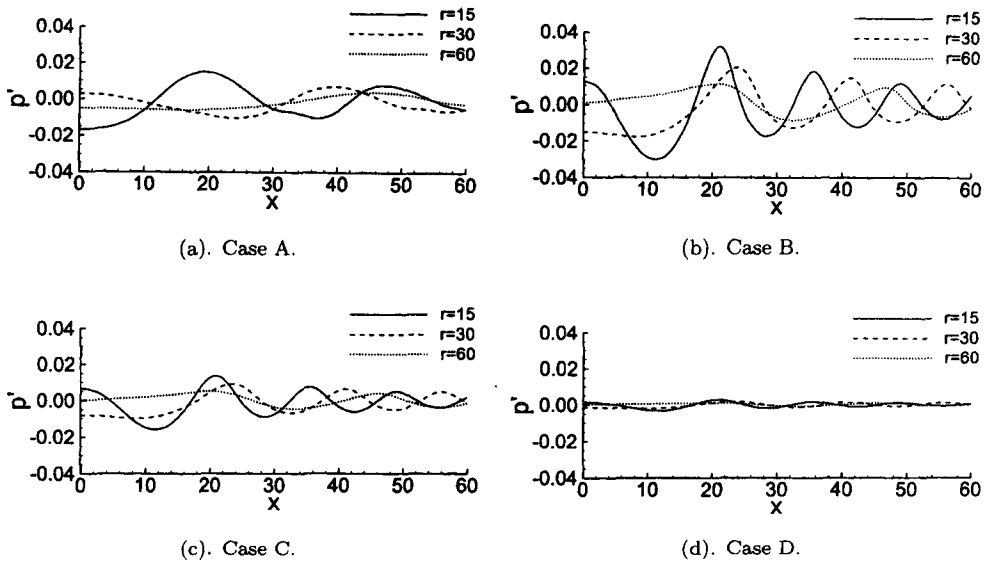

(a). Case A. (b). Case B.

(c). Case C. (d). Case D.

Figure 7. Instantaneous pressure fluctuation profiles of Cases A–D at $t = 200$.

From Figure 7, it is evident that the sound wavelength of Cases B, C, and D is approximately half of that of Case A, due to the fact that the sound frequency of Case A is half of that of Cases B, C, and D (shown in Figure 9). The sound wavelength for Case A is approximately $30r_0$, while the sound wavelength for Cases B, C, and D is approximately $15r_0$. From Figure 7, it can be seen that the instantaneous sound pressure can be positive or negative depending on the local pattern of the sound wave propagation. In Figure 7, it is evident that the pressure fluctuation amplitude decays with the increase of radial distance. The pressure fluctuation amplitude also decays slightly in the streamwise direction.

To further examine the sound field characteristics of the heated pulsating jet, Figure 8 shows time traces of the sound at three fixed points ($x = 15$, $r = 15$), ($x = 30$, $r = 30$) and ($x = 60$, $r = 60$), for Cases A–D. It can be observed that the sound arrives at the downstream locations at progressively later time. For all the cases shown in Figure 8, it is noticed that the pressure fluctuation amplitude at ($x = 30$, $r = 30$) is about half of that at ($x = 15$, $r = 15$), while the pressure fluctuation amplitude at ($x = 60$, $r = 60$) is about half of that at ($x = 30$, $r = 30$). Assuming the sound source is located at the jet nozzle exit (shown in Figure 11), this implies that the pressure fluctuation amplitude of the pulsating jet is inversely proportional to the distance from the noise source. This agrees well with the acoustic theory that states the amplitude of pressure fluctuations decreases in inverse proportion to the distance from the sound source in a free space [1,27]. From Figure 8, it is also observed that, among the four cases, the largest sound pressure variation occurs for Case B with 100% pulsation and with the pulsating frequency of $f_0 = 0.2$. Comparing Figures 8a and 8b, it is noticed that the pressure fluctuation amplitude of Case A is about 50% of that of Case B, albeit with the fact that these two cases have the same 100% pulsating amplitude at the inflow. This indicates that the higher pulsating frequency in Case B leads to a stronger sound radiation in this case than that in Case A with the lower pulsating frequency $f_0 = 0.1$. Comparing Figures 8b, 8c, and 8d, it can be seen that the pressure fluctuation amplitude decreases with the decrease of pulsating amplitude. The pressure fluctuation amplitude is approximately proportional to the pulsating amplitude. The pressure fluctuation amplitude of Case C with 50% velocity pulsation is about half of that of Case B with 100% pulsation, while the pressure fluctuation amplitude of Case D with 10% velocity pulsation is about 20% of that of Case C. This implies that there is approximately a linear relationship between pressure fluctuation amplitude and pulsating amplitude in the pulsating jet.

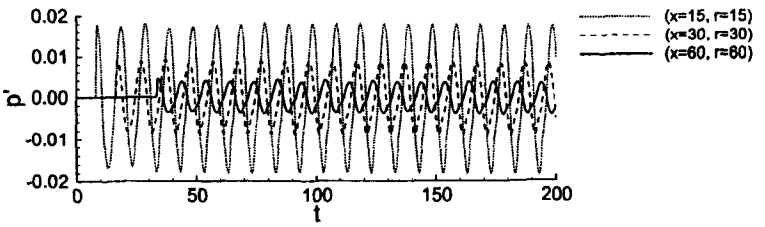

(a). Case A.

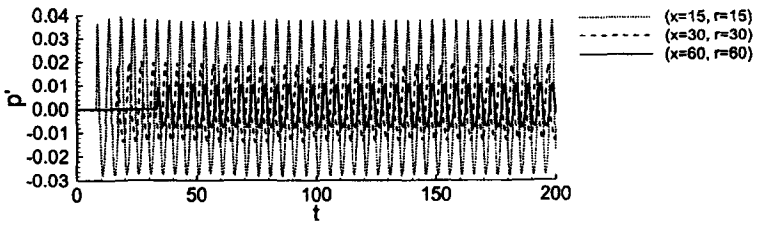

(b). Case B.

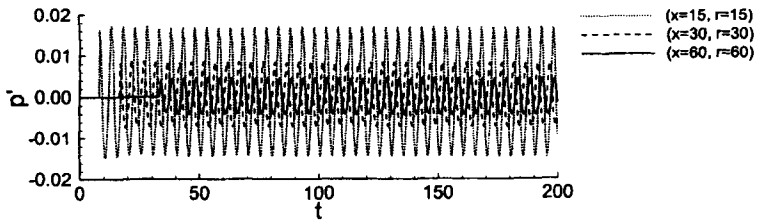

(c). Case C.

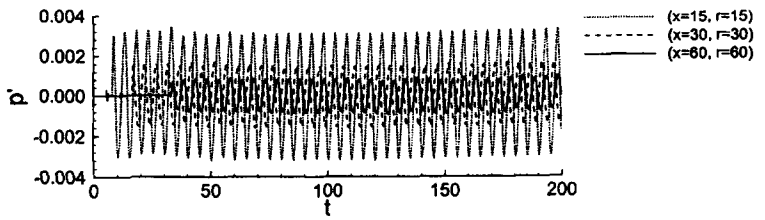

(D). Case D.

Figure 8. Pressure fluctuation histories at ($x = 15$, $r = 15$), ($x = 30$, $r = 30$), and ($x = 60$, $r = 60$) of Cases A–D.

A close examination of Figure 8 reveals that the pulsating periods of the sound pressure are almost the same at the three locations for each of the computational case. To clarify this, Figure 9 shows the Fourier spectra of the sound pressure histories of the four cases, for the three locations shown in Figure 8. From Figure 9, it is clear that the sound field of the pulsating jet is dominated by the velocity pulsating frequency supplied at the inflow and it does not contain appreciable higher frequencies. This is mainly due to the axisymmetric nature of the simulations and the large pulsation applied at the inflow boundary. In idealized axisymmetric simulations, high frequency turbulence could not develop due to the lack of vortex breakdown that would have been developed in a fully three-dimensional turbulent jet. For the sound field, there is no obvious spectrum broadening and observable Doppler shift in frequency. No Doppler shift means stationary sound source. For Cases C and D, the sound field frequency has not been affected by the vortex pairing. This is mainly because that the sound source (shown in Figure 11) is located upstream of the vortex pairing location, therefore the vortex pairing does not have a strong influence on frequency of the sound field. In Figure 9, the effects of pulsating amplitude and frequency on the

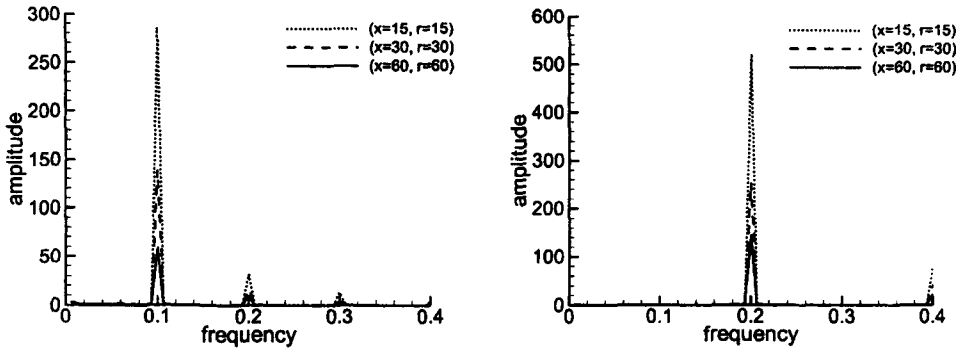

(a). Case A. (b). Case B.

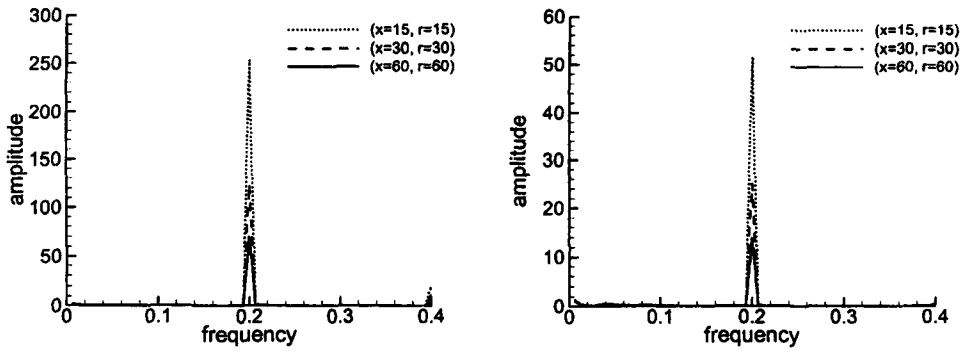

(c). Case C. (d). Case D.

Figure 9. Fourier spectra of the pressure fluctuation histories at (x = 15, r = 15), (x = 30, r = 30), and (x = 60, r = 60) of Cases A–D.

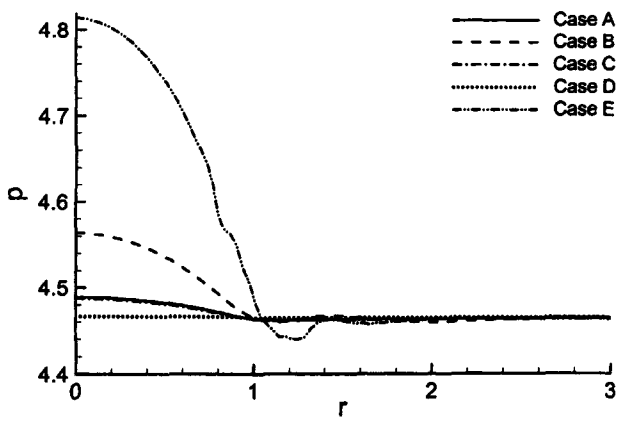

Figure 10. The time-averaged pressure profiles at x = 0 of Cases A–E.

pressure fluctuation amplitude and frequency of the radiated sound field of the pulsating jet are evident. The pressure fluctuation amplitude of the sound field is approximately proportional to the pulsating amplitude and frequency. It is also inversely proportional to the distance from the sound source.

3.2. Time-Averaged Flow and Sound Characteristics

In this study, time averaging of the simulation results has been performed to examine the time-averaged flow properties, sound source structure and sound fields of the pulsating jet. The

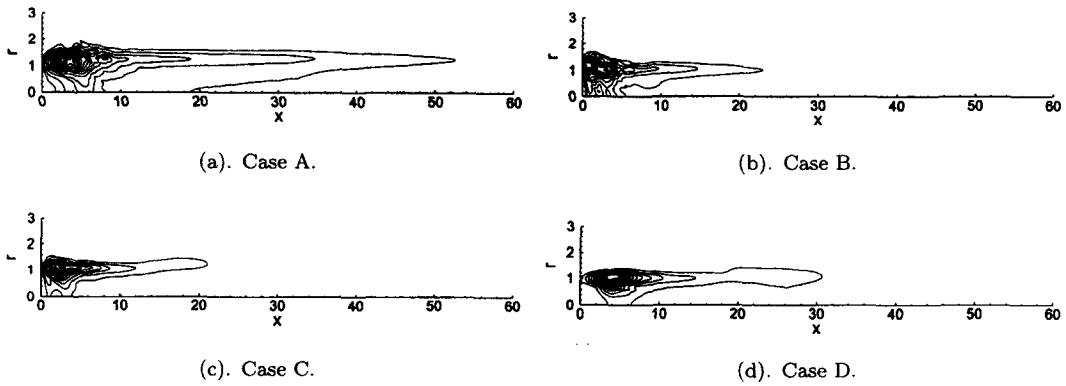

(a). Case A. (b). Case B.

(c). Case C. (d). Case D.

Figure 11. Contours of the root-mean-square of the sound source of Cases A–D (15 contours between the minimum and maximum values).

time interval used for the averaging is between $t_1 = 140$ and $t_2 = 200$, after the flow has reached a fully developed periodic stage. Figure 10 shows comparisons of the time-averaged pressure profiles at the jet nozzle exit for the five cases performed. For the pulsating jet, the accumulation of transient compression and expansion waves near the jet nozzle exit due to the applied velocity pulsation leads to pressure changes in this region. In Figure 10, the pressure radial profiles at the jet nozzle exit for Cases A and C are almost overlapping. From Figure 10, it is evident that the larger pulsating frequency and larger pulsating amplitude lead to more underexpanded flow near the nozzle exit, which is characterized by high pressures. This is because that the flow accumulates more energy near the jet nozzle exit at high pulsating frequency and pulsating amplitude, which leads to the formation of a more underexpanded flow field in this region [8].

Vortical structures in jet shear layers act as sound source. The velocity pulsation at the inflow (jet nozzle exit) can also act as sound source. An advantage offered by DNS as a tool of CAA is that it yields the complete vortical flow field and the exact structure of the sound source, which are hard to obtain from experimental measurements. In this study, the statistical sound source distributions have been calculated to examine the sound generation mechanisms from the pulsating jet. The right-hand side of equation (9) is considered to be the sound source. Instantaneously, its value can be positive or negative. To examine the statistical sound source distribution, contours of the root-mean-square (rms) of the sound source of Cases A–D are shown in Figure 11. It can be seen that the intense sound source is located in the jet shear layer close to the jet nozzle exit. The acoustic source has a long axial length in the streamwise flow direction. Among the four cases, the sound source of Case B is the strongest and closest to the jet nozzle exit due to the fact that this case has the strongest vorticity very close to the nozzle exit in comparison with the other three cases. In general, the sound source moves closer to the jet nozzle exit with increased pulsating frequency and amplitude. It is also found that the sound source becomes stronger but shorter in the streamwise direction when the pulsating frequency or amplitude is increased.

To quantitatively examine the sound field of the heated pulsating jet, the sound pressure level has also been calculated in this study, based on the time-averaged sound field properties obtained. The sound pressure level is a dimensional quantity and the measurement units are decibels (dB). The dimensional sound pressure level (dB) can be calculated from the following equation [1],

$$L_p^* = 20 \cdot \log_{10} \frac{p'_{\text{rms}} p^*_{\text{ref}}}{20 \times 10^{-6}} = 20 \cdot \log_{10} \frac{1.01325 \times 10^5 \gamma M^2 p'_{\text{rms}}}{20 \times 10^{-6}}. \tag{12}$$

In equation (12), p'_{rms} represents the nondimensional root-mean-square pressure fluctuation, the superscript $*$ represent dimensional quantities. In obtaining the above equation, the standard reference pressure 20μPa has been taken as the hearing threshold for calculating the sound

pressure level [1], while the ambient pressure has been taken as 1.01325×10^5Pa. Based on the definition of sound pressure level, the theoretical equation linking the sound pressure levels at two different points in the sound field is

$$L_{p2}^* = L_{p1}^* - 10 \cdot \log_{10} \left(\frac{R_2}{R_1} \right)^2. \tag{13}$$

In equation (13), R is the distance to the sound source. Assuming that the sound source is located at the center of the jet nozzle exit, it can be expressed as $R = \sqrt{x^2 + r^2}$ for the axisymmetric jet. The theoretical correlation given in equation (13) implies that the sound pressure level measured at increasing distances in a free space decreases by approximately 6 dB for each doubling of distance [1].

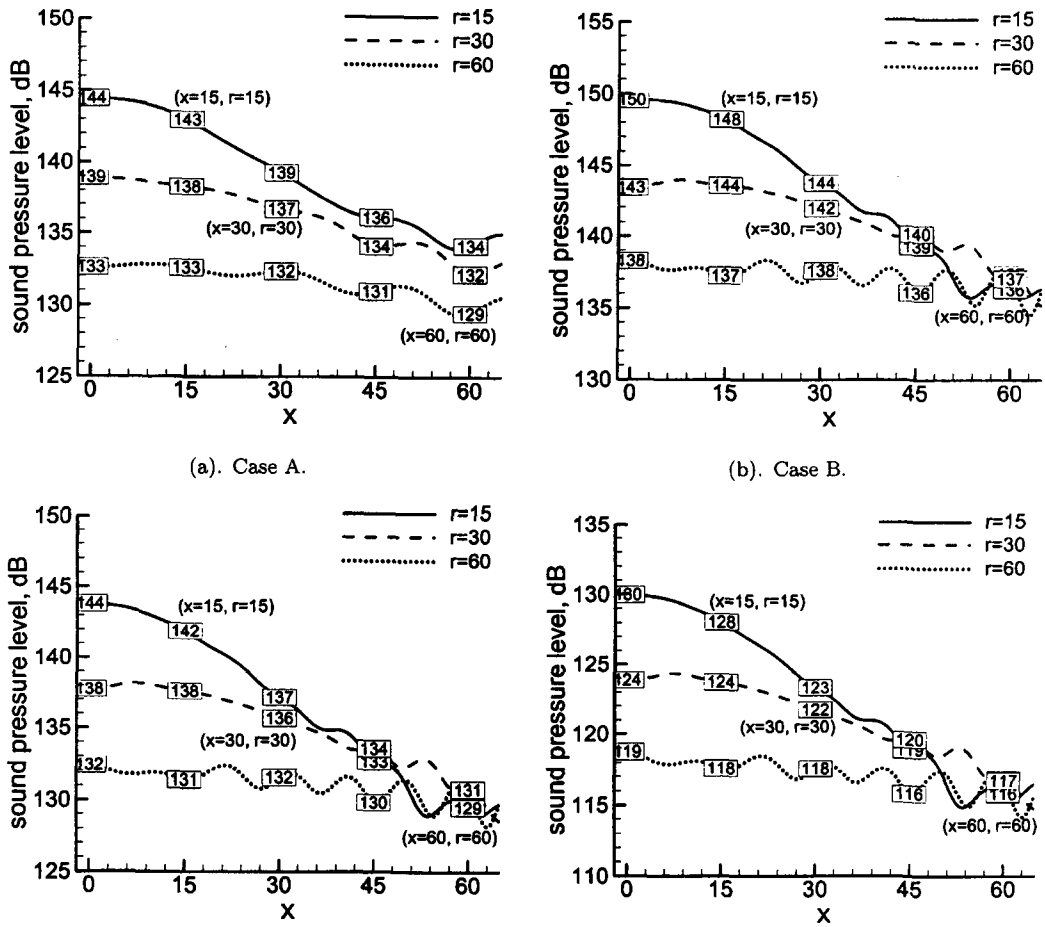

(a). Case A.

(b). Case B.

(c). Case C.

(d). Case D.

Figure 12. Profiles of the sound pressure level at $r = 15$, $r = 30$, and $r = 60$ of Cases A–D.

Figure 12 shows profiles of the sound pressure level of Cases A–D at three different radial locations: $r = 15$, $r = 30$, and $r = 60$, respectively. It can be seen that the sound pressure level of the heated axisymmetric pulsating jet is quite high. Among the four cases, Case B has the highest sound pressure level and Case D has the lowest sound pressure level, while the sound pressure level of Cases A and C are close to each other. From Figure 12, it is observed that the sound pressure level decreases with the increase of radial distance. It also decreases in

the streamwise direction. These trends are consistent with those observed previously from the instantaneous pressure fluctuations. To compare the simulation results with acoustic theory, the three fixed points ($x = 15$, $r = 15$), ($x = 30$, $r = 30$) and ($x = 60$, $r = 60$) in the sound field with sequentially doubling distance from the jet nozzle exit have been marked in Figure 12. From this figure, it can be observed that the computed sound pressure level of the heated pulsating jet decreases approximately by 6 dB for each doubling of distance, which is in good agreement with the acoustic theory [1]. A close examination of the three points on the jet inlet plane ($x = 0$, $r = 15$), ($x = 0$, $r = 30$), and ($x = 0$, $r = 60$) reveals the same trend. This agreement achieved with acoustic theory qualitatively validates the direct computation of the sound field of heated axisymmetric pulsating jet performed in this study. The simulation results are believed to be accurate due to the nondissipative sixth-order numerical scheme [15] used. The dispersion error from the numerical scheme is also believed to be small since a large number of grid points were used and no numerical oscillations were observed in the flow and sound fields. The fluctuation of the sound pressure level shown in Figure 12 is mainly because that the sound source of the heated axisymmetric pulsating jet is located in the jet upstream region and the sound field is highly directive. Since experimental data under the same flow conditions are not available in the literature, a direct comparison between the simulated data and experimental measurements is not possible. While no direct comparisons with experimental results are presented, the computed results are in agreement with acoustic theory, including the distance dependence of the pressure fluctuation amplitude and sound pressure level.

4. CONCLUDING REMARKS

Detailed characteristics of the sound generated by a heated axisymmetric pulsating jet have been numerically explored by solving the compressible Navier-Stokes equations using highly accurate numerical methods. Effects of pulsating frequency and amplitude on the flow structure and sound generation of the subsonic jet have been examined by parametric axisymmetric simulations. The simulations performed are instantaneously axisymmetric; therefore, three-dimensional instabilities have been inhibited. The strictly axisymmetric jet simulated in this study differs from a fully three-dimensional turbulent jet that is axisymmetric in its mean flow due to the lack of small-scale turbulence in the simulations performed. A direct comparison between the simulated data and experimental measurements with the same flow conditions is not possible. However, the trends observed from the numerically predicted sound field agree well with the acoustic theory. The axisymmetric simulations performed are considered as "building blocks" for the study of fully three-dimensional pulsating turbulent flows. Due to the qualitative agreement achieved with acoustic theory, conclusions on the effects of pulsating frequency and amplitude on the unsteady dynamic behaviour and sound generation are believed to be general that are not expected to change in a fully three-dimensional turbulent pulsating jet.

The simulation results have revealed that the organized unsteadiness associated with the periodic velocity pulsation leads to a variety of vortical structures in the pulsating jet flow field. Depending on the pulsating frequency and amplitude, different vortical structures have been observed. The pulsating jet develops larger vortices at the lower pulsating frequency. For the effects of pulsating amplitude, it has been observed that vortex pairing occurs at relatively low pulsating amplitudes. It is also observed that the larger pulsating amplitude and pulsating frequency lead to more underexpanded flows near the jet nozzle exit. The analysis of the sound source has revealed that the intense sound source is located in the jet shear layer close to the jet nozzle exit. The sound source becomes stronger with increased pulsating frequency and amplitude and it decays faster in the streamwise direction when the pulsating frequency or amplitude is increased. It is shown that the sound source distribution is influenced by both the pulsating frequency and amplitude. The pulsating frequency and amplitude also influence the sound propagation; therefore have strong effects on sound field of the pulsating jet.

The effects of pulsating frequency and amplitude on sound fields radiated from the heated axisymmetric pulsating jet have been examined. It has been observed that the sound field generated by the heated pulsating jet is highly directive. At the higher pulsating frequency, the jet radiated sound field has smaller wavelength compared with the sound field of a jet with the lower pulsating frequency. The results show that the pressure fluctuation amplitude is inversely proportional to the distance from the sound source. Both the larger pulsating frequency and larger pulsating amplitude lead to stronger sound emissions from the heated pulsating jet. More importantly, it has been observed from the direct computation that the pressure fluctuation amplitude of the sound field of the pulsating jet is approximately proportional to the pulsating amplitude and frequency. The distance dependence shown in the numerically predicted pressure fluctuation amplitude of the sound field is in good agreement with acoustic theory and the predicted sound pressure level is in adequate agreement with the theoretical deduction.

REFERENCES

1. R. Farnell and D. Riding, Engine noise, In *Diesel Engine Reference Book*, Second Edition, (Edited by B. Challen and R. Baranescu), pp. 485–507, Butterworth-Heinemann, Oxford, (1999).
2. S. Walker, Larger engine noise and vibration control, In *Diesel Engine Reference Book*, Second Edition, (Edited by B. Challen and R. Baranescu), pp. 509–519, Butterworth-Heinemann, Oxford, (1999).
3. A. Onorati, Numerical simulation of unsteady flows in internal combustion engine silencers and the prediction of tailpipe noise, In *Design Techniques for Engine Manifolds—Wave Action Methods for IC Engines*, (Edited by D.E. Winterbone and R.J. Pearson), pp. 267–340, Professional Engineering Publishing Limited, London, (1999).
4. J.O. Keller, P.A. Eibeck, T.T. Bramlette and P.K. Barr, Pulse combustion—Tailpipe exit jet characteristics, *Combust. Sci. Technol.* **94**, 167–192, (1993).
5. G. Raman and D. Cornelius, Jet mixing control using excitation from miniature oscillating jets, *AIAA J.* **33**, 356–368, (1995).
6. A. Eroglu and R.E. Breidenthal, Structure, penetration, and mixing of pulsed jets in crossflow, *AIAA J.* **39**, 417–423, (2001).
7. Y. Hardalupas and A. Selbach, Imposed oscillations and non-premixed flames, *Prog. Enery. Combust.* **28**, 75–104, (2002).
8. A. Kimura and J. Iwamoto, A study on generation of noise by high-speed pulsating jets, *Journal of Visualization* **5**, 371–379, (2002).
9. P.O.A.L. Davies and K.R. Holland, I.C. engine intake and exhaust noise assessment, *J. Sound Vib.* **223**, 425–444, (1999).
10. X. Jiang, E.J. Avital and K.H. Luo, Sound generation from vortex pairing in subsonic coaxial jets, In *Proceedings of the 10th International Congress on Sound and Vibration, pp. 3875–3882*, Royal Institute of Technology (KTH), Stockholm, Sweden, (2003).
11. X. Jiang, E.J. Avital and K.H. Luo, Direct computation and aeroacoustic modelling of a subsonic axisymmetric jet, *J. Sound Vib.* **270**, 525–538, (2004).
12. X. Jiang, E.J. Avital and K.H. Luo, Sound generation by vortex pairing in subsonic axisymmetric jets, *AIAA J.* **42**, 241–248, (2004).
13. G.M. Lilley, The generation and radiation of supersonic jet noise, In *Report AFAPL TR-72-53, Volume 4*. U.S. Air Force Aero Propulsion Laboratory, (1972).
14. J.H. Williamson, Low-storage Runge-Kutta schemes, *J. Comput. Phys.* **35**, 48–56, (1980).
15. S.K. Lele, Compact finite-difference schemes with spectral-like resolution, *J. Comput. Phys.* **103**, 16–42, (1992).
16. K.W. Thompson, Time dependent boundary conditions for hyperbolic systems, *J. Comput. Phys.* **68**, 1–24, (1987).
17. B.E. Mitchell, S.K. Lele and P. Moin, Direct computation of the sound generated by vortex pairing in an axisymmetric jet, *J. Fluid Mech.* **383**, 113–142, (1999).
18. A. Michalke, Survey on jet instability theory, *Prog. Aerosp. Sci.* **21**, 159–199, (1984).
19. F.M. White, *Viscous Fluid Flow*, McGraw-Hill, New York, (1974).
20. T.J. Poinsot and S.K. Lele, Boundary conditions for direct simulations of compressible viscous flows, *J. Comput. Phys.* **101**, 104–129, (1992).
21. S.C. Crow and F.H. Champagne, Orderly structure in jet turbulence, *J. Fluid Mech.* **48**, 547–591, (1971).
22. A.K.M.F. Hussain and K.B.M.Q. Zaman, The preferred mode of the axisymmetric jet, *J. Fluid Mech.* **110**, 39–71, (1981).
23. W. Zhao and S.H. Frankel, Numerical simulations of sound radiated from an axisymmetric premixed reacting jet, *Phys. Fluids* **13**, 2671–2681, (2001).
24. N.D. Sandham, The effect of compressibility on vortex pairing, *Phys. Fluids* **6**, 1063–1072, (1994).

25. C. Cerretelli and C.H.K. Williamson, The physical mechanism for vortex merging, *J. Fluid Mech.* **475**, 41–77, (2003).
26. D.G. Crighton and P. Huerre, Shear-layer pressure fluctuations and superdirective acoustic sources, *J. Fluid Mech.* **220**, 355–368, (1990).
27. P.E. Doak, An introduction to sound radiation and its sources, In *Noise and Acoustic Fatigue in Aeronautics*, (Edited by E.J. Richards and D.J. Mead), pp. 1–42, Wiley, London, (1968).